Check for updates

Beyond structural insight: a deep neural network for the prediction of Pt L$_{2/3}$-edge X-ray absorption spectra†

Luke Watson, [ID] Conor D. Rankine [ID] and Thomas J. Penfold [ID] *

X-ray absorption spectroscopy at the L$_{2/3}$ edge can be used to obtain detailed information about the local electronic and geometric structure of transition metal complexes. By virtue of the dipole selection rules, the transition metal L$_{2/3}$ edge usually exhibits two distinct spectral regions: (i) the "white line", which is dominated by bound electronic transitions from metal-centred 2p orbitals into unoccupied orbitals with d character; the intensity and shape of this band consequently reflects the d density of states (d-DOS), which is strongly modulated by mixing with ligand orbitals involved in chemical bonding, and (ii) the post-edge, where oscillations encode the local geometric structure around the X-ray absorption site. In this Article, we extend our recently-developed XANESNET deep neural network (DNN) beyond the K-edge to predict X-ray absorption spectra at the Pt L$_{2/3}$ edge. We demonstrate that XANESNET is able to predict Pt L$_{2/3}$ -edge X-ray absorption spectra, including both the parts containing electronic and geometric structural information. The performance of our DNN in practical situations is demonstrated by application to two Pt complexes, and by simulating the transient spectrum of a photoexcited dimeric Pt complex. Our discussion includes an analysis of the feature importance in our DNN which demonstrates the role of key features and assists with interpreting the performance of the network.

1 Introduction

Interest in machine learning (used as an umbrella term for a variety of statistical algorithms that build predictive or decision-capable models based on inferences from data) has surged in recent years as a consequence of fundamental advances in deep learning algorithms [especially deep neural networks (DNNs)],[1] the increased accessibility of high-performance computational hardware, and the proliferation of large data sets.[2–4] In chemistry,[5] machine-learning models have the potential to be able to make fast, accurate, and affordable predictions of properties and observables, sometimes with very little external input, and they are consequently very appealing for a broad range of applications including materials,[6–10] catalyst,[11–14] and drug design,[15,16] chemical reaction prediction,[17–21] and atomistic modelling.[22–27]

Spectroscopy is central to research across the natural sciences and in engineering, being one of the most effective methods for characterising the properties of molecules and

materials. This has led to the development of a number of approaches aimed at exploiting machine learning for data reduction, prediction, and/or analysis, in addition to accelerating theoretical calculations of electronically-excited states and spectra.[28–42] In particular, and the focus of this Article, the X-ray regime provides valuable element- and site-specific information on the geometric, electronic, and spin structure of matter and, consequently, a number of recent works have addressed directly the development of models for the prediction and analysis of X-ray absorption spectra.[43–65]

These approaches can be subdivided into two categories: (i) "forward" (*i.e.* property/structure-to-spectrum) and (ii) "reverse" (*i.e.* spectrum-to-property/structure) mappings. The latter is perhaps the more natural of the two, in some sense, as it has a clear connection to the problem that X-ray spectroscopists face day-to-day in their work: how can a measurement/observable be interpreted? However, direct extraction of three-dimensional structure in the "reverse" mapping approach cannot be achieved without constraints due to the limited resolution of X-ray spectra and, consequently, most approaches have focused on deriving key structural parameters, *e.g.* oxidation state, coordination number, or morphology, among others. In addition, for the analysis of complicated, disordered, and dynamical systems, it is very unlikely that deriving a single three-dimensional structure from an X-ray

Chemistry – School of Natural and Environmental Sciences, Newcastle University, Newcastle, upon Tyne, NE1 7RU, UK. E-mail: tom.penfold@ncl.ac.uk

† Electronic supplementary information (ESI) available. See https://doi.org/10.1039/d2cp00567k

9156 | *Phys. Chem. Chem. Phys.*, 2022, **24**, 9156–9167

This journal is © the Owner Societies 2022

spectrum would be physically meaningful. In such a situation, high-throughput (*i.e.* fast, accurate, and affordable) theory is needed to enable large-scale configurational sampling using the "forward" mapping approach.

To address this, we have recently developed[43,47] and applied[45,46] a deep neural network (DNN) based on the simple multilayer perceptron (MLP) model that has been able to model accurately and affordably the K-edge X-ray absorption spectra of transition metal complexes. Our DNN predicts peak positions with sub-eV accuracy and peak intensities with errors over an order of magnitude smaller than the spectral variations that the model is engineered to capture from no input beyond geometric information about the local environment of the X-ray absorption site.[43,47] With the ability to predict *ca.* 1000 XANES spectra per second using off-the-shelf commercial-grade hardware (an AMD Ryzen Threadripper 3970X CPU; 3.7–4.5 GHz), our DNN provides a significant reduction in computational expense compared to first-principles/*ab initio* simulations that facilitates large-scale configurational sampling. In the context of the present work, it is important to note that transition metal K-edge XANES spectra are dominated by post-edge oscillations relating directly to structural features *via* the scattering of X-ray photoelectrons (Fig. 1a). In contrast, by virtue of the dipole selection rules, transition metal $L_{2/3}$ edge XANES spectra, especially those corresponding to 5 d elements such as Pt, as studied here, usually exhibit two distinct spectral regions: (i) the "white line", which is dominated by bound electronic transitions from metal-centred 2p orbitals into unoccupied orbitals with *d* character; the intensity and shape of this band consequently reflects the *d* density of states (*d*-DOS), which is strongly modulated by mixing with ligand orbitals involved in chemical bonding, and (ii) the post-edge, where oscillations encode the local geometric structure around the X-ray absorption site (Fig. 1b).

In this Article, we extend our recently-developed DNN[43,47] beyond the K-edge to predict XANES spectra at the Pt $L_{2/3}$ edge with a view towards exploring whether it is possible for the present framework to predict accurately the electronic, as well as the structural, features of the $L_{2/3}$ edge. Importantly, although there has been significant development in the first-principles/*ab initio* treatment of $L_{2/3}$ edge XANES spectra,[66–73] it remains a challenging task to develop (statistical) model-based approaches. While (machine-learning) models for K-edge X-ray spectroscopy are advancing at pace, fewer model-based approaches have been developed to target the $L_{2/3}$ edge. Recent work by Lueder is one such example, which has seen the introduction of models structured around a multiplet-theory-based approach and demonstrated that they are effective for predicting $L_{2/3}$-edge X-ray absorption spectra for first-row transition metal complexes.[74,75] Through the use of multiplet theory, Lueder's approach focused on the electronic, rather than structural, components of the $L_{2/3}$ edge XANES spectra.[74,75] We demonstrate that our DNN, trained on theoretical spectra, and using local geometric information around the absorption site, is able to predict Pt $L_{2/3}$ edge XANES spectra including both the parts dominated by electronic and geometric structural information. The performance of our DNN in a practical situation is demonstrated by application to two Pt complexes and by prediction of the transient spectrum of a dimeric Pt complex. Our discussion includes an analysis of the feature importance in our DNN which demonstrates the role of key features and assists with interpreting the performance of the network.

2 Theory and computational details

2.1 Dataset and multiple scattering theory calculations

Our reference dataset comprises Pt X-ray absorption site geometries ("samples") derived from 6530 Pt-containing structures harvested from the transition metal Quantum Machine (tmQM)[76,77] dataset with the corresponding $L_{2/3}$ edge XANES spectra ("labels") calculated in-house using multiple scattering
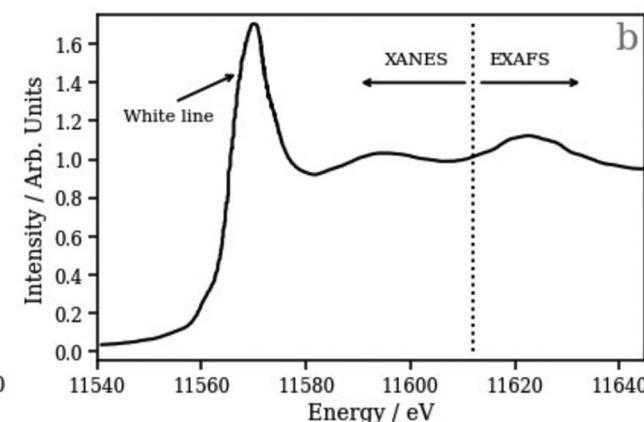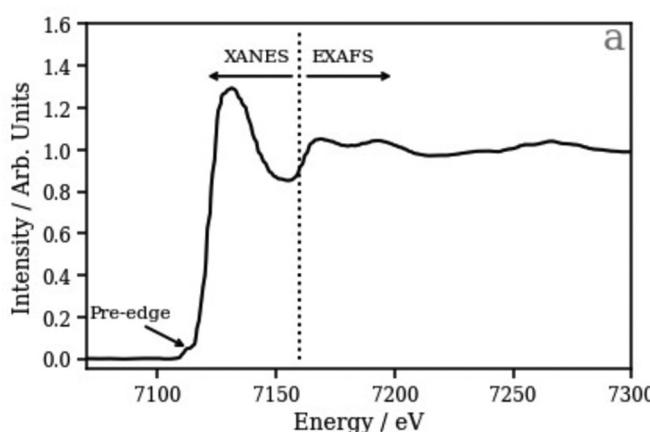

Fig. 1 (a) A typical transition metal (Fe) K-edge X-ray absorption spectrum; weak pre-edge features, arising from dipole-forbidden 3d ← 1s transitions, are indicated and the X-ray absorption near-edge structure (XANES) and extended X-ray absorption fine structure (EXAFS) regions of the spectrum are demarcated. (b) A (Pt) L_3 edge X-ray absorption spectrum; the "white line", arising from dipole-allowed 5d ← 2p transitions, is indicated and the XANES and EXAFS regions of the spectrum are demarcated.

This journal is © the Owner Societies 2022

Phys. Chem. Chem. Phys., 2022, **24**, 9156–9167 | **9157**

theory (MST) as implemented in the FDMNES package.[78,79] 530 samples from the reference dataset were isolated at random to form a "held-out" testing dataset (evaluated post-optimisation only). The remaining samples comprised the training and validation datasets used during optimisation. The average $L_{2/3}$ edge XANES spectra and the variance over this subset of samples is shown in Fig. S1 (ESI†). The training and validation subsets were constructed "on-the-fly" throughout *via* repeated K-fold cross validation with five repeats and five folds, *i.e.* a five-times-repeated 80 : 20 split.

The Pt $L_{2/3}$-edge XANES MST calculations employed a self-consistent muffin-tin-type potential of radius 6.0 Å around the X-ray absorbing site, and the interaction with the X-ray field was described using the electric quadrupole approximation. Relativistic effects, including spin–orbit coupling (SOC; implemented following the approach of Wood and Boring in ref. 80) were integrated into the Pt $L_{2/3}$ edge XANES MST calculations to split the L_2 and L_3 edges.

In this Article, three different sets of target XANES spectra were used, each differing in the preprocessing applied to the calculated absorption cross-sections. The first case, where the absorption cross-sections were used as obtained from FDMNES without any preprocessing, we refer to as the unconvoluted/non-broadened model. The second case, where the calculated absorption cross-sections were convoluted/broadened with a simple, fixed-width Lorentzian function [full-width-at-half-maximum (FWHM) = 0.5 eV], we refer to as the Lorentzian-broadened model. The final case, which represents the typical preprocessing strategy for theoretical spectra, we refer to as the arctan-broadened model; here, the calculated absorption cross-sections were convoluted with an energy-dependent arctangent function to account for various factors including the core-hole-lifetime broadening, instrument response, and many-body effects, *e.g.* inelastic losses. This particular kind of convolution was carried out following an empirical model close to the Seah–Dench formalism[81] as detailed in ref. 43. All reference datasets associated with this work are publicly available; refer to the Data Availability Statement for details.

2.2 Deep neural network

The general architecture of the current-generation XANESNET DNN is described in detail in ref. 47 we recommend this reference to the unfamiliar reader. The code is publicly available under the GNU Public License (GPLv3) on GitLab.[82]

Briefly, the architecture is based on the deep multilayer perceptron (MLP) model and comprises an input layer, two hidden layers, and an output layer. All layers are dense, *i.e.* fully connected, and each hidden layer performs a nonlinear transformation using the rectified linear unit (relu) activation function. The input layer comprises 129 neurons (to accept a feature vector of 129 symmetry functions encoding the local environment around an X-ray absorption site), the hidden layers each comprise 512 neurons, and the output layer comprises 1100 neurons from which the discretised $L_{2/3}$ edge XANES spectrum is retrieved, *i.e.* XANESNET is a multi-output MLP with each output neuron corresponding to the spectral

intensity at a given energy gridpoint. The inputs – local environments around X-ray absorption sites – are encoded *via* dimensionality reduction using the weighted atom-centered symmetry function (wACSF) descriptor of Gastegger and Marquetand *et al.*[83]

The internal weights, **W**, are optimised *via* iterative feedforward and backpropagation cycles to minimise the empirical loss, $J(\mathbf{W})$, defined here as the mean-squared error (MSE) between the predicted, $\mu_{predict}$, and target, μ_{target}, $L_{2/3}$ -edge XANES spectra. Gradients of the empirical loss with respect to the internal weights, $\delta J(\mathbf{W})/\delta\mathbf{W}$, were estimated over minibatches of 32 samples and updated iteratively according to the Adaptive Moment Estimation (ADAM) algorithm. The learning rate for the ADAM algorithm was set to 1×10^{-4}.

Regularization was implemented to minimize the propensity of overfitting; batch standardization and dropout were applied at each hidden layer. The probability, p, of dropout was set to 0.25.

The XANESNET DNN is programmed in Python 3 with the TensorFlow[84]/Keras[85] API and integrated into a Scikit-Learn[86] (sklearn) data pre- and post-processing pipeline *via* the Keras-Regressor wrapper for Scikit-Learn. The Atomic Simulation Environment[87] (ase) API is used to handle and manipulate molecular structures.

3 Results and discussion

3.1 Deep neural network evaluation

Fig. 2a and b show the relative performance of our DNN (*i.e.* the percentage difference in the performance of the model relative to the best-performing model for that figure panel) at the Pt L_2 and L_3 edges, respectively, as a function of number of training cycles ("epochs"). We have evaluated three models which differ in the way that the $L_{2/3}$ edge XANES spectra are preprocessed, *i.e.* in the choice of target function (see Theory and computational details).

The first (the "unconvoluted/non-broadened" model) is optimised with the calculated absorption cross-section as the target function. As shown in Fig. S2 (ESI†), these target functions exhibit sharp resonances characteristic of bound–bound (*e.g.* d ← 2p) transitions, especially in the region close to the X-ray absorption edge, arising from the high density of 5d ← 2p transitions. At the Pt L_2 and L_3 edges, this model shows very limited, near-negligible improvement (<10%) as a function of the number of epochs (Fig. 2). This is a consequence of the challenges that our DNN faces in learning the multitude of sharp resonances in the pre-edge and around the "white line". Indeed, in the simple MLP model, each individual neuron in the output layer of a multi-output network is independent; here, each represents a discretised energy point in the Pt $L_{2/3}$ edge XANES spectrum (see Theory and computational details). However, the narrow nature of these resonances means that small spectral shifts can transfer the entire intensity from one output neuron to another. From the perspective of our DNN, this represents a very large change in the target output, but it is

9158 | *Phys. Chem. Chem. Phys.*, 2022, **24**, 9156–9167

This journal is © the Owner Societies 2022
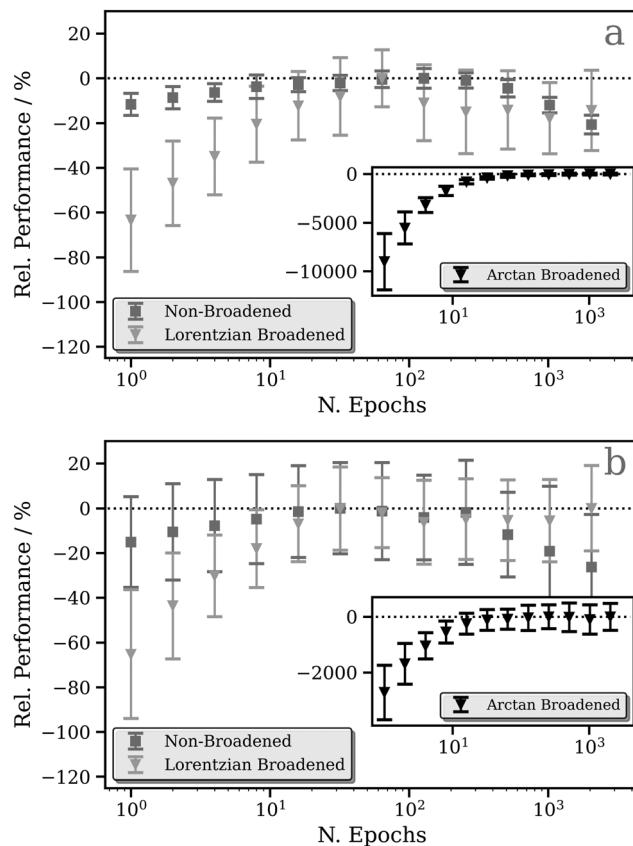
Fig. 2 Relative performance of the DNN at the Pt L_2 (a) and L_3 (b) edges as a function of the number of training cycles ("epochs"). Three models are shown, differing in their choice of target function: the target functions used are (i) the calculated absorption cross-section (without any post-processing), (ii) the calculated absorption cross-section broadened with a fixed-width Lorentzian function (FWHM = 0.5 eV), and (iii) the calculated absorption cross-section broadened with an arctangent convolution model (see Theory and computational details). Data points are averaged over 100 K-fold cross-validated evaluations; error bars indicate one standard deviation.

in fact one that could be induced with a very small change in the input – the local geometric structure around the absorption site. This can lead to a breakdown in the correlation between inputs (*i.e.* structures) and outputs (*i.e.* spectra) reducing the effectiveness of learning. In addition, the objective of the DNN during training is to minimise the loss/cost function (here, the MSE; see Theory and computational details); given the challenges of modelling the sharp resonances in the pre-edge and around the "white line", the DNN focuses on this region throughout training as it has the largest effect on the MSE. This can lead to poorer performance for predictions of the above-ionisation resonances in the post-edge. On this basis, we conclude that this first model is inappropriate for the Pt $L_{2/3}$ edge (*cf.* the situation at the K edge; see ref. 43), and so we discard it at this point – we will not consider it again in this Article.

To address this situation, a second model was optimised with fixed-width-Lorentzian-broadened (FWHM = 0.5 eV) absorption cross-sections as the target functions. This second

model shows a stronger improvement as a function of the number of epochs; a *ca.* 60% improvement is observed at the Pt L_2 (Fig. 2a) and L_3 (Fig. 2b) edges. A third model was also optimised (inset in Fig. 2) in which the calculated absorption cross-sections were preprocessed *via* broadening with the energy-dependent arctangent function described in ref. 43. Illustrative example spectra can be seen in Fig. S2 (ESI†). This third model shows a much greater relative change in performance as a function of the number of epochs, likely a consequence of the lower resolution of the target function post-convolution. The average MSE converges towards *ca.* 1.0×10^{-4} and, given that the MSE from the first few epochs (*ca.* 1.0×10^{-2}) is orders of magnitude greater, this model consequently exhibits a huge percentage-wise improvement in performance at the Pt L_2 (Fig. 2a) and L_3 (Fig. 2b) edges.

Focusing on the fixed-width-Lorentzian- and arctan-broadened models, Fig. 3 shows the relative performance of our DNN as a function of the number of samples in the training dataset. For both the fixed-width-Lorentzian- (Fig. 3a) and arctan-broadened (Fig. 3b) models, a percentage-wise improvement of *ca.* 50% is
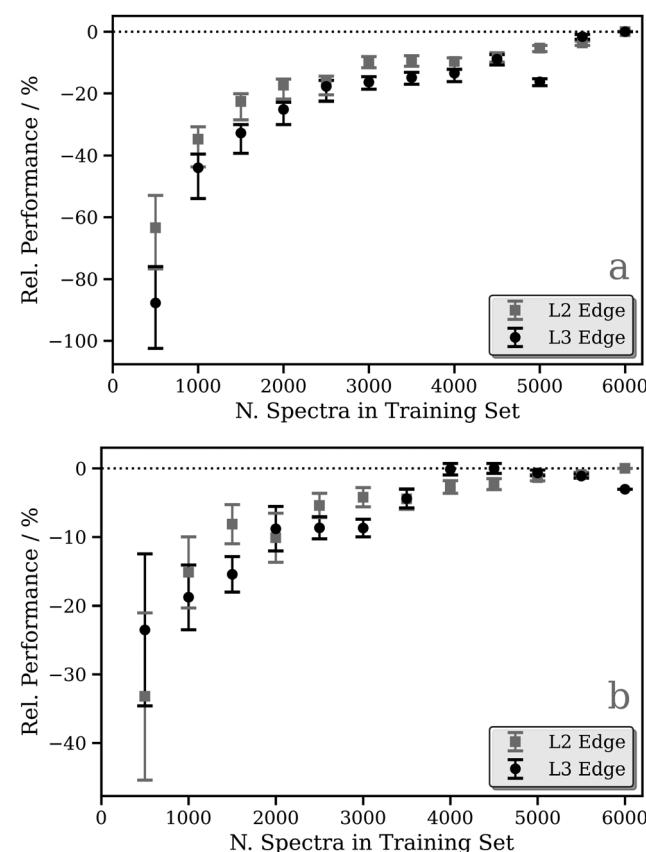

Fig. 3 Relative performance of the DNN as a function of the number of samples in the training dataset. The corresponding target functions are (a) the calculated absorption cross-sections broadened with a fixed-width Lorentzian function (FWHM = 0.5 eV) and (b) the calculated absorption cross-sections broadened with an arctangent convolution model (see Theory and computational details). Data points are averaged over 100 K-fold cross-validated evaluations; error bars indicate one standard deviation.

This journal is © the Owner Societies 2022

Phys. Chem. Chem. Phys., 2022, **24**, 9156–9167 | **9159**

observed over an increase in the size of the training set from *ca.* 500 to 6000 samples. A comparable improvement is observed for both the Pt L_2 and L_3 edges. Fig. S3–S6 (ESI†) show six DNN-predicted and theoretical Pt $L_{2/3}$ edge XANES spectra presented for the purpose of comparison; in each Figure, the upper and lower three panels contain selections from the top and bottom 1% of DNN predictions, respectively, where predictions are ranked by MSE. In both the Lorentzian- and arctan-broadened models, the top 1% of DNN predictions are essentially indistinguishable from the target Pt L_2 and L_3 edge XANES spectra.

Fig. 4a and c show percentage error between the target and the actual spectrum achieved on DNN predictions of Pt L_2 and L_3 edge XANES spectra, respectively, for the 530 held-out samples in the testing dataset. Here, the absorption cross-sections have been broadened with a fixed-width Lorentzian function (FWHM = 0.5 eV); the corresponding data for the absorption cross-sections broadened with the energy-dependent arctangent function are shown in Fig. S7 (ESI†). For the Pt L_2 edge (Fig. 4a), the median percentage error is 4.827, and the lower and upper quartiles are found at 6.386 and 8.080, respectively, while for the Pt L_3 edge (Fig. 4c), the median percentage error is 4.605, and the lower and upper quartiles are found at 6.013 and 7.973, respectively. In Fig. 4b and d, bar charts of the median percentage error point-by-point are overlaid on averaged Pt L_2 and L_3 edge XANES spectra, respectively. These figures show that the error is largest in the region of the spectrum near the edge/"white line". This is likely the consequence of two primary factors: (i) the edge/"white line"

region of the spectrum is the most structured and, therefore, the most challenging for the DNN, and (ii) the input, *i.e.* the local (geometric) environment around the X-ray absorption site, is purely structural and does not encode electronic information (*e.g.* orbital structure) directly. One would expect this additional information to be valuable for predictions in this region of the XANES spectrum given the electronic nature of the resonances (*cf.* the above-ionisation resonances in the post-edge).

3.2 Predicting the Pt $L_{2/3}$ edge XANES of zerovalent Pt complexes

A key application of $L_{2/3}$ edge XANES is to probe directly, by virtue of the dipole selection rules, the unoccupied d valence orbitals, which can provide insight into the electronic structure and chemical bonding framework of the complex under study. One example from organometallic chemistry is to interpret chemical bonding within the framework of the Dewar–Chatt–Duncanson model,[88,89] *i.e.* in the context of σ donation and π back-donation between the transition metal and the ligands. Indeed, transition metal $L_{2/3}$ edge XANES has been used to describe the bonding in organometallic complexes within this framework in a number of previous studies.[90–92]

Here, we test the performance of our DNN by predicting the Pt L_3 edge XANES spectra of two zerovalent Pt molecules:[93,94] [Pt(PH$_3$)$_2$ (η^2-C$_2$H$_4$)] and [Pt(PH$_3$)$_2$ (η^2-C$_2$ (CN)$_4$)] (shown in Fig. 5a and b, respectively). As previously demonstrated by Dias, Fonseca, and Herbst,[95] the "white lines" of these spectra are an effective measure of the π* strength of the C$_2$H$_4$ and C$_2$
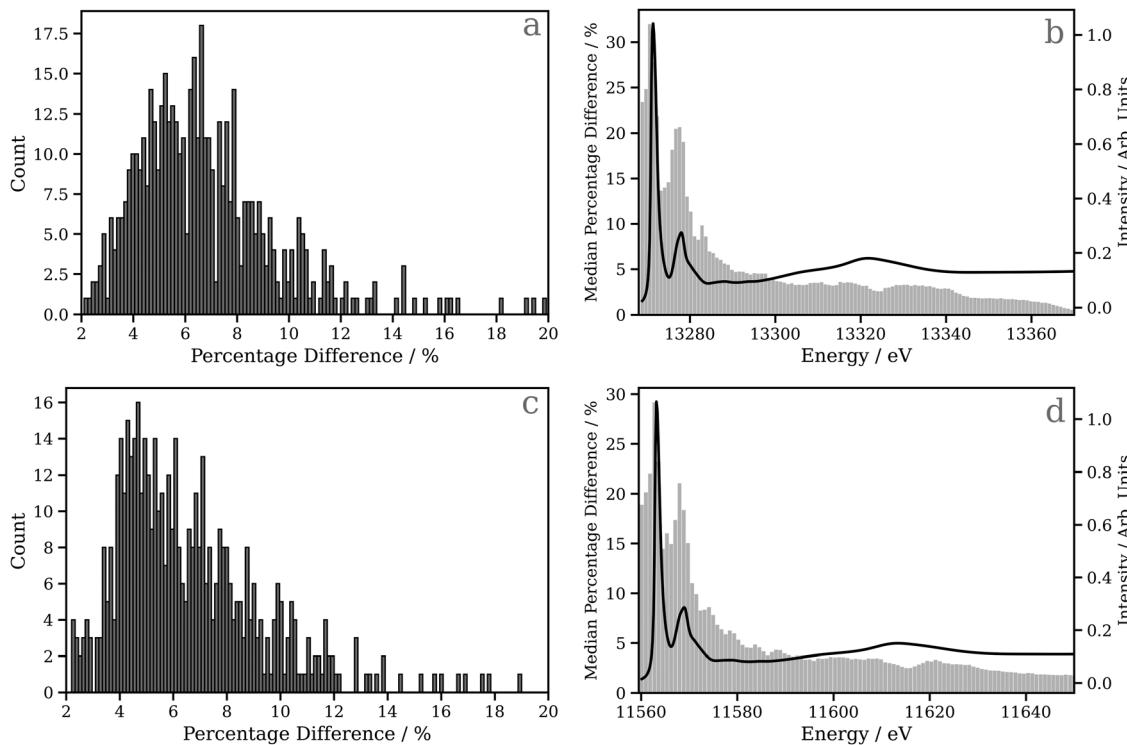

Fig. 4 Histograms of the percentage error between the target and the actual spectrum achieved on 530 held-out DNN predictions of Pt $L_{2/3}$ edge XANES spectra, and bar charts of the median percentage error point-by-point overlaid with an averaged Pt $L_{2/3}$ edge XANES spectrum (black trace); (a) and (b) are for the Pt L_2 edge, and (c) and (d) are for the Pt L_3 edge.

a) $[Pt(PPh_3)_2(\eta^2\text{-}C_2H_4)]$

(Front View)

(Side View)

b) $[Pt(PPh_3)_2(\eta^2\text{-}C_2(CN)_4)]$ c) $[Pt(ppy)(\mu\text{-}^tBu_2pz)]_2$
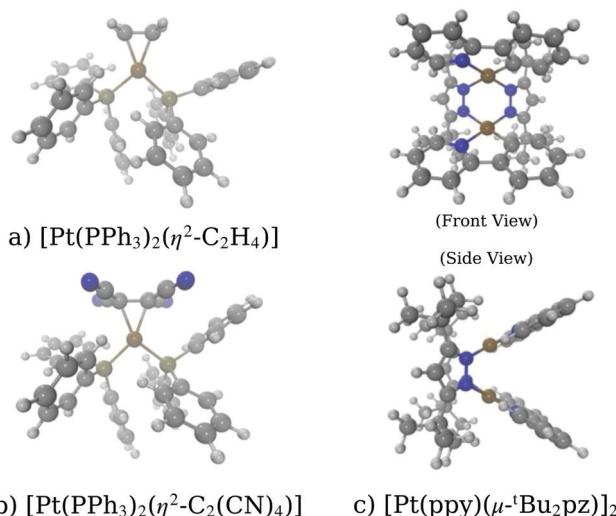
Fig. 5 Schematics of the molecules studied in the work: (a) $[Pt(PH_3)_2\ (\eta^2\text{-}C_2H_4)]$, (b) $[Pt(PH_3)_2\ (\eta^2\text{-}C_2(CN)_4)]$, and (c)$[Pt(ppy)(\mu\text{-}^tBu_2\ pz)]_2$.

$(CN)_4$ ligands coordinated to the $Pt(PPh_3)_2$ fragment. Fig. 6 shows Pt L_3 edge DNN predictions (solid lines) for $[Pt(PH_3)_2\ (\eta^2\text{-}C_2H_4)]$ and $[Pt(PH_3)_2\ (\eta^2\text{-}C_2(CN)_4)]$ compared to the experimental Pt L_3 edge XANES spectra (dashed lines). For both $[Pt(PH_3)_2\ (\eta^2\text{-}C_2H_4)]$ and $[Pt(PH_3)_2\ (\eta^2\text{-}C_2(CN)_4)]$, strong
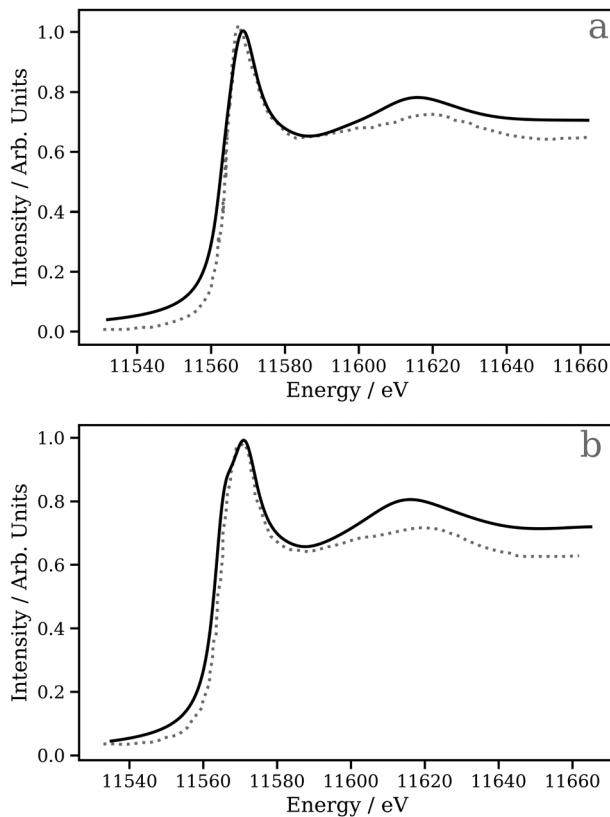
Fig. 6 The Pt L_3 edge XANES spectra of (a) $[Pt(PH_3)_2\ (\eta^2\text{ -}C_2H_4)]$ and (b) $[Pt(PH_3)_2\ (\eta^2\text{ -}C_2(CN)_4)]$. The dashed lines are experimental Pt L_3 edge XANES spectra digitised from ref. 95 and the solid lines are DNN predictions.

qualitative agreement of the spectral shape is observed with both the edge and post-edge resonances captured, albeit with the latter being slightly too intense in the Pt L_3 -edge DNN predictions relative to the experimental traces. In terms of the electronic properties of the complexes, the Pt 5d-DOS can be interpreted using the edge jump (E_0; located at the inflection point of the rising edge) and the edge maximum (E_{max}) of the "white line". If we assume, as in the aforementioned work,[95] that E_0 reflects the energy of the highest-occupied molecular orbital (HOMO) and E_{max} reflects the energy of the lowest-unoccupied molecular orbital (LUMO), the HOMO–LUMO gap can be estimated as $E_{max} - E_0$.[96,97] In addition - because the aforementioned work[95] has established that the HOMO is dominated by Pt dπ-orbitals and the LUMO by π^* orbitals for these complexes – this energy difference can be related to the dπ-orbital interaction energy, ΔE_π, and manifests as a doublet growth in the second derivative of the spectra shown for the DNN predictions in Fig. S8 (ESI†). ΔE_π, as determined from our DNN predictions, is found to be *ca.* 4 and 6 eV for $[Pt(PH_3)_2\ (\eta^2\text{-}C_2H_4)]$ and $[Pt(PH_3)_2\ (\eta^2\text{-}C_2(CN)_4)]$, respectively; values that are in excellent agreement with their experimentally-determined counterparts: *ca.* 4 and 7 eV for $[Pt(PH_3)_2\ (\eta^2\text{-}C_2H_4)]$ and $[Pt(PH_3)_2\ (\eta^2\text{-}C_2(CN)_4)]$, respectively.[95]

A deeper understanding can be provided by a "shell-by-shell"[98,99] simulation (a simulation in which the number of neighboring atoms around the X-ray absorption site is gradually increased by incorporating an increasing number of radial "shells" up to the point of convergence) which also provides, in parallel, an opportunity to assess the performance of our DNN compared to first-principles/*ab initio* simulations carried out using the FDMNES package (*i.e.* does our model capture the expected physics?). Fig. 7a and b show the "shell-by-shell" simulation for $[Pt(PH_3)_2\ (\eta^2\text{-}C_2(CN)_4)]$ using FDMNES and our DNN, respectively. Increasing the radius from 2 Å to 4 Å and, ultimately, 6 Å leads to a reduction of the "white line" intensity and an increase in intensity of the post-edge resonance at *ca.* 11 610 eV. The change in the "white line" intensity reflects the mixing of the Pt d-DOS with ligand orbitals, which serves to broaden and, consequently, reduce the spectral intensity. The change in the post-edge resonance occurs from scattering from the surrounding ligands. The changes observed in the first-principles/*ab initio* FDMNES simulations are captured consistently and qualitatively well by our DNN, which is encouraging.

The ability of our DNN to capture the correct behaviour in the "shell-by-shell" simulation depends, to an extent, on the sensitivity of each radial (G^2-type) input feature in the wACSF feature vector (see Theory and computational details). Fig. 7c and d show plots of the inference feature importance for the individual G^2-type symmetry functions at the Pt L_2 and L_3 edges, respectively, obtained by assessing the performance penalty (Rel. Performance) when randomising the input featurewise, *i.e.* each point represents one of the 64 G^2 type symmetry functions in the wACSF feature vector, and the relative performance hit when randomising that feature reflects the evaluated importance of the feature to the DNN at inference time. A similar trend is observed at the Pt L_2 and L_3 edges, with

This journal is © the Owner Societies 2022

Phys. Chem. Chem. Phys., 2022, **24**, 9156–9167 | **9161**
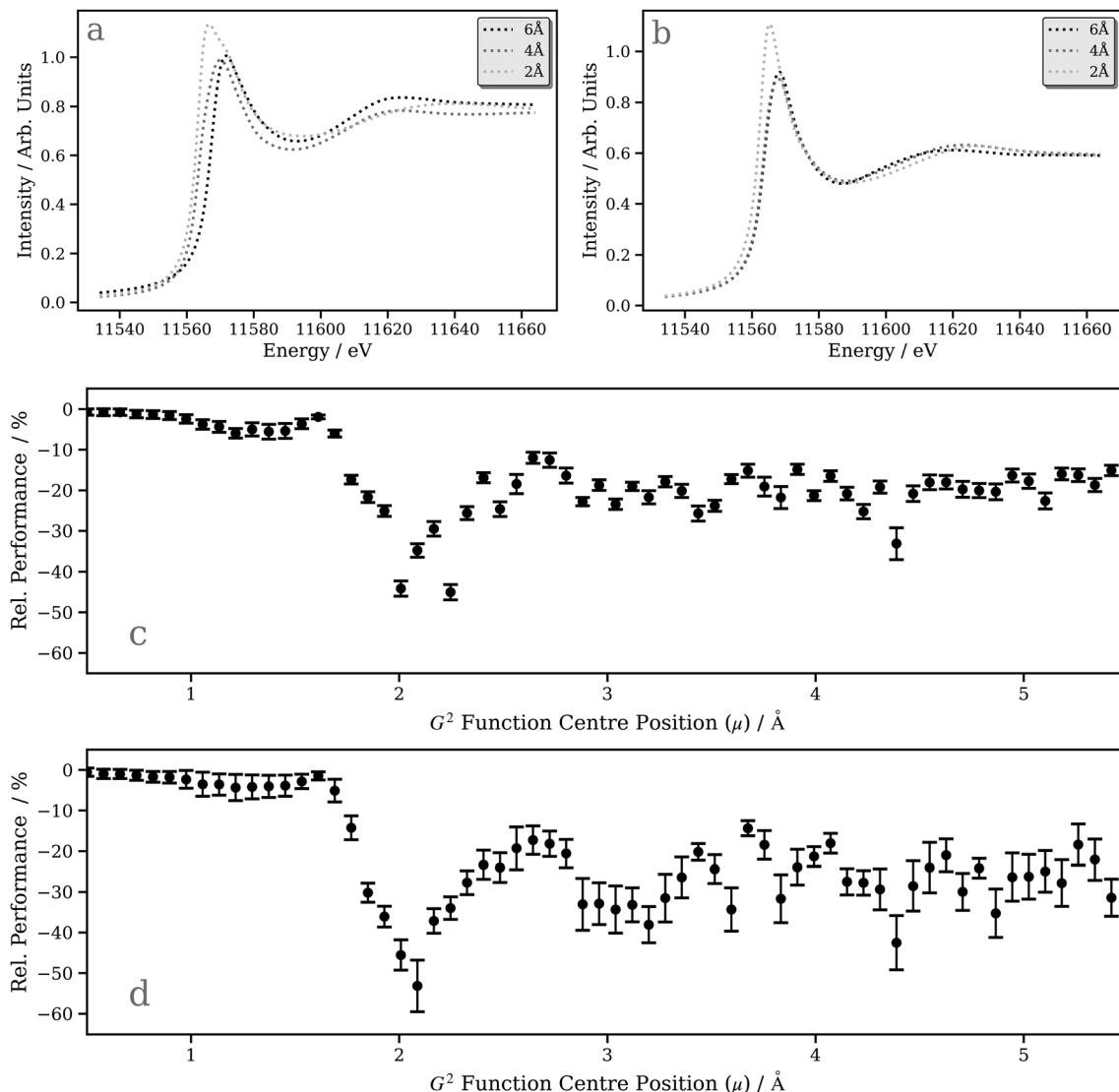
Fig. 7 Pt L$_3$-edge XANES spectra derived from an (a) FDMNES and (b) DNN "shell-by-shell" simulation of [Pt(PH$_3$)$_2$ (η^2-C$_2$(CN)$_4$)] as a function of the shell cutoff radius around the absorption site, and plots of the (inference) feature importance for the individual G^2-type symmetry functions at the (c) Pt L$_2$ and (d) L$_3$ edges obtained by assessing the (negative) percentage change in model performance when randomising the input featurewise.

the strongest sensitivity observed at *ca.* 2–3 Å. This corresponds approximately to the first and second coordination spheres for the Pt-containing organometallic complexes in the tmQM[76,77] dataset. It consequently explains the strong change observed when expanding the shell from 2 to 4 Å in the DNN "shell-by-shell" simulation and the weaker effect when expanding the shell from 4 to 6 Å (Fig. 7b).

3.3 Predicting the effect of excited-state distortions in a Pt dimer

In this second case study, we focus on the excited-state structure of a dinuclear Pt(II) complex with *tert*-butyl substituted pyrazolate bridging units: [Pt(ppy)(μ-^{t}Bu$_2$pz)]$_2$ (Fig. 5c; ppy = 2-phenylpyridine; ^{t}Bu$_2$pz = 3,5-di-*tert*-butylpyrazolate) – a complex previously studied by Lockard *et al.*[100] Indeed, there has been extensive work carried out using time-resolved X-ray techniques on diplatinum transition metal complexes with a

view towards elucidating the electronic and geometric structural changes upon photoexcitation.[66,101–104]

Fig. 8a shows the Pt L$_3$ edge XANES spectrum of [Pt(ppy)(μ-^{t}Bu$_2$pz)]$_2$ in the electronic ground state. The DNN prediction reproduces the shape of the experimental Pt L$_3$ edge XANES spectrum with good qualitative agreement in terms of position and intensity, particularly in the "white-line" region yet, although the energetic position of the post-edge resonance is in good agreement with experiment, it is slightly too intense. One potential reason for this is that [Pt(ppy)(μ-^{t}Bu$_2$pz)]$_2$, having two Pt atoms, is irregular given the content of the training dataset (otherwise exclusively mono-Pt complexes); predictions for [Pt(ppy)(μ-^{t}Bu$_2$pz)]$_2$ could be considered to be beyond the scope of the present model. To investigate this possibility, Fig. 8c is presented; a violin plot of the distribution of G^2-type symmetry function values included within the training set is shown in this figure, and the scatter markers show the G^2-type symmetry

9162 | *Phys. Chem. Chem. Phys.*, 2022, **24**, 9156–9167

This journal is © the Owner Societies 2022
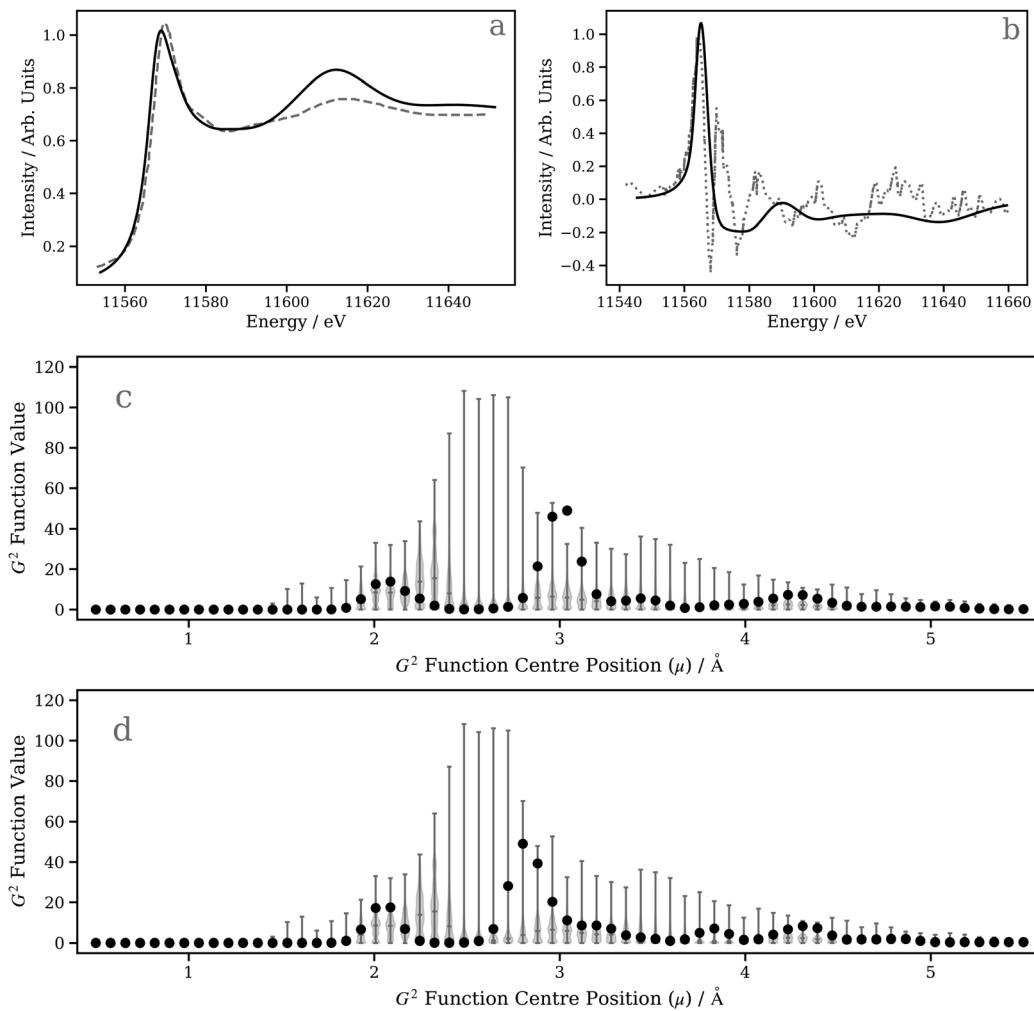
Fig. 8 (a) Pt L_3-edge XANES spectrum of [Pt(ppy)(μ-^{t}Bu$_2$pz)]$_2$ in the ground state. (b) Transient Pt L_3 edge XANES spectrum of [Pt(ppy)(μ-^{t}Bu$_2$ pz)]$_2$ (S$_0$–T$_1$). (c) Violin plot of the distribution of G^2-type symmetry function values present in the training data with medians and extrema indicated; filled circles correspond to the G^2-type symmetry function values for the wACSF vector describing [Pt(ppy)(μ-^{t}Bu$_2$pz)]$_2$ in the S$_0$ state. (d) Violin plot of the distribution of G^2-symmetry function values present in the training data with medians and extrema indicated; filled circles correspond to the G^2 -type symmetry function values for the wACSF vector describing [Pt(ppy)(μ-^{t}Bu$_2$ pz)]$_2$ in the T$_1$ state.

function values associated with the wACSF vector describing [Pt(ppy)(μ-^{t}Bu$_2$pz)]$_2$ at the electronic ground-state geometry. Fig. 8c shows that the G^2 symmetry functions describing the environment at an *ca.* 3 Å radial distance (corresponding to the Pt–Pt distance) are at the edge of, or outside, the range of values found in the training dataset, which could suggest that the model may be less reliable here. For reference, Fig. S9 (ESI†) shows a histogram of atom types and their respective distances from the Pt X-ray absorption sites in the training dataset used in this work.

Fig. S10 (ESI†) shows the influence of the second Pt atom on the DNN predictions and first-principles/*ab initio* FDMNES simulations. For the latter, there is limited effect. While this may be surprising, it is nonetheless consistent with previous analysis on a diplatinum system[66] which showed that the spectral feature at 11.610 keV is not strongly affected by the second Pt atom but, instead, results from scattering from the first and second coordination shells around each Pt X-ray

absorption site.[66] In contrast, the DNN predictions show a large reduction in intensity in this feature when removing the second Pt atom, illustrating the effect of its presence is overestimated in our present model – again, likely because it differs considerably from the content of our current training dataset.

Next, we investigate the transient Pt L_3 edge XANES spectrum, *i.e.* the difference XANES spectrum between the excited-state and ground-state Pt L_3 edge XANES spectra.[105,106] This represents a larger challenge for our DNN as both spectra have to be described accurately in order to reproduce the experimentally-acquired transient. Fig. 8b shows both the experimentally-acquired and DNN-predicted transient Pt L_3 edge XANES spectra. The experimental XANES spectrum (digitised from ref. 100) was acquired 100 ps post-photoexcitation of [Pt(ppy)(μ-^{t}Bu$_2$pz)]$_2$ with 527 nm light at a time after which the complex is expected to have relaxed into its lowest-energy triplet (T$_1$) excited state.[100] The first positive feature in the experimentally-acquired transient (located at *ca.* 11565 eV) arises from a 5d ← 2p electronic

This journal is © the Owner Societies 2022

Phys. Chem. Chem. Phys., 2022, **24**, 9156–9167 | **9163**

transition driven by the photoexcitation, while the remaining features observed in the experimentally-acquired transient reflect structural changes.[100] As observed in Fig. 8b, our DNN-predicted transient is in poor agreement with the experimentally-acquired transient and, above the positive transition at *ca.* 11560 eV, shows only very weak changes. It is possible to rationalise this from Fig. 8d, which not only shows that the G^2-type symmetry function values encoding information on the Pt–Pt distance for the T_1-state complex are at the edge of range of values contained in the training dataset (and, in any case, dinuclear Pt complexes are not contained in the training dataset), but – crucially – that the change in Pt–Pt distance post-photoexcitation moves the interaction into a region where our DNN is less sensitive to changes in geometry [*i.e.* the feature importance is comparatively low around *ca.* 2.5–2.7 Å (T_1 state) as opposed to *ca.* 2.9–3.1 Å (S_0 state); Fig. 7c and d]. Compounding the difficulties faced here, the structural changes of the complex otherwise are small (≤ 0.03 Å). We therefore expect that the inadequate simulation of the experimentally-acquired transient is largely due to these factors, and this dinuclear Pt(II) complex clearly falls outside the scope of the presently-developed model.

4 Conclusions

In this Article, we have developed and applied a DNN to predict accurately and affordably Pt $L_{2/3}$-edge XANES spectra. In contrast to our previous work[43–47] at the transition metal K edges, the $L_{2/3}$-edge XANES spectra exhibit a larger and more direct sensitivity to the electronic structure of the absorbing atom owing to the dipole-allowed bound–bound 5d $\leftarrow$ 2p electronic transitions. In contrast, at the transition metal K-edges, electronic transitions into the unoccupied d-DOS are dipole forbidden and form only a weak pre-edge region in the K-edge XANES spectra. This has brought into focus a key question: does our input representation, based entirely on the geometric structure, remain reliable and encode the necessary information for a 'forward' mapping of the structure onto the $L_{2/3}$-edge XANES spectral features?

We have demonstrated that, using a small training dataset of 6000 local absorption sites and Pt $L_{2/3}$-edge XANES spectra, it is possible to develop a DNN with a simple architecture, very similar to our previous transition metal K-edge DNNs,[43,47] which is effective for predicting Pt $L_{2/3}$ edge XANES spectra, as demonstrated on 530 held-out testing dataset samples. However, a key difference from our previous work[43–47] at the transition metal K edges is that, here, our DNN is ostensibly unable to learn from absorption cross-sections without preprocessing since the $L_{2/3}$ edge exhibits very structured, sharp resonance peaks characteristic of bound-bound transitions. This challenge is addressable by applying either a fixed-width Lorentzian or arctangent convolutional broadening to each calculated $L_{2/3}$ edge XANES spectrum prior to training. While both show effective learning, the latter option is the less desirable of the two as it presumes a specific (instrument) resolution, while this can (and generally does) vary between

different experimental techniques [*e.g.* when using high-energy-resolution fluorescence detection (HERFD)[107] spectroscopy]. Consequently, to maintain the generality of our DNN at the $L_{2/3}$ edge, we have focused on the former preprocessing strategy for training the model and, as for the transition metal K edges, made available the option to apply a tailored artangent convolutional broadening as an post-processing step.

In terms of the performance of our DNN at the Pt $L_{2/3}$ edge, we have shown that the largest percentage differences are observed in the "white line"/edge region of the XANES spectrum: the part which is dominated by electronic transitions and is probably poorly predicted without explicit electronic information being supplied to our DNN. This potentially highlights a limitation of our current encoding strategy: it is based entirely on geometric information about the local environment around the absorption site. At the transition metal K edge, the majority of the features in the XANES spectrum are above-ionisation resonances which arise through interferences of the scattered X-ray photoelectrons and, here, the direct link to between structure and spectrum (necessary for a physical 'forward' mapping) is clear. In contrast, at the $L_{2/3}$ edge, there is a substantially larger contribution from electronic characteristics and, while there is still an implicit link between the geometric properties of the local environment around the absorption site and the electronic structure of the complex, it is not as direct.

We applied our DNN to two test examples: (i) predicting the Pt $L_{2/3}$-edge XANES of zerovalent Pt complexes, and (ii) predicting the Pt $L_{2/3}$-edge transient corresponding to excited-state distortions in a Pt dimer. For the latter, we demonstrated that when poor agreement between our DNN predictions and the experimentally-acquired transient arose, this could be traced back to the details of the model and, in particular, the contents of the training dataset. Indeed, any artificial learning model will only ever be as good as the data used to train it. Consequently, future work in this area needs to focus on bespoke training datasets for (transition metal) X-ray absorption spectroscopy, tailored to maximise the sensitivity of the model(s) to the particular problem(s).[108]

Data availability

The data supporting this publication are openly available under an Open Data Commons Open Database License. Additional metadata are available at 10.25405/data.ncl.17206706.

Conflicts of interest

There are no conflicts to declare.

Acknowledgements

9164 | *Phys. Chem. Chem. Phys.*, 2022, **24**, 9156–9167

This journal is © the Owner Societies 2022

Notes and references

1 Y. Lecun, Y. Bengio and G. Hinton, *Nature*, 2015, **521**, 436–444.

2 M. I. Jordan and T. M. Mitchell, *Science*, 2015, **349**, 255–260.

3 S. Shalev-Shwartz and S. Ben-David, *Understanding Machine Learning: From Theory to Algorithms*, Cambridge University Press, 2014.

4 M. Mohri, A. Rostamizadeh and A. Talwalkar, *Foundations of Machine Learning*, MIT Press, 2018.

5 A. C. Mater and M. L. Coote, *J. Chem. Inf. Model.*, 2019, **59**, 2545–2559.

6 K. T. Schütt, H. Glawe, F. Brockherde, A. Sanna, K.-R. Müller and E. K. Gross, *Phys. Rev. B: Condens. Matter Mater. Phys.*, 2014, **89**, 205118.

7 B. Meredig, A. Agrawal, S. Kirklin, J. E. Saal, J. W. Doak, A. Thompson, K. Zhang, A. Choudhary and C. Wolverton, *Phys. Rev. B: Condens. Matter Mater. Phys.*, 2014, **89**, 094104.

8 K. T. Butler, D. W. Davies, H. Cartwright, O. Isayev and A. Walsh, *Nature*, 2018, **559**, 547–555.

9 W. Sun, Y. Zheng, K. Yang, Q. Zhang, A. A. Shah, Z. Wu, Y. Sun, L. Feng, D. Chen and Z. Xiao, *et al.*, *Sci. Adv.*, 2019, **5**, eaay4275.

10 S. Chibani and F.-X. Coudert, *APL Mater.*, 2020, **8**, 080701.

11 Z. Li, X. Ma and H. Xin, *Catal. Today*, 2017, **280**, 232–238.

12 Z. Li, S. Wang, W. S. Chin, L. E. Achenie and H. Xin, *J. Mater. Chem. A*, 2017, **5**, 24131–24138.

13 J. R. Kitchin, *Nat. Catal.*, 2018, **1**, 230–232.

14 A. F. Zahrt, J. J. Henle, B. T. Rose, Y. Wang, W. T. Darrow and S. E. Denmark, *Science*, 2019, **363**, eaau5631.

15 R. Burbidge, M. Trotter, B. Buxton and S. Holden, *Compr. Chemom.*, 2001, **26**, 5–14.

16 V. D. Mouchlis, A. Afantitis, A. Serra, M. Fratello, A. G. Papadiamantis, V. Aidinis, I. Lynch, D. Greco and G. Melagraki, *Int. J. Mol. Sci.*, 2021, **22**, 1676.

17 M. H. Segler and M. P. Waller, *Chem. – Eur. J.*, 2017, **23**, 5966–5971.

18 J. S. Schreck, C. W. Coley and K. J. Bishop, *ACS Cent. Sci.*, 2019, **5**, 970–981.

19 V. H. Nair, P. Schwaller and T. Laino, *CHIMIA Int. J. Chem.*, 2019, **73**, 997–1000.

20 D. P. Kovács, W. McCorkindale and A. A. Lee, *Nat. Commun.*, 2021, **12**, 1–9.

21 P. Schwaller, A. C. Vaucher, T. Laino and J.-L. Reymond, *Mach. Learn.: Sci. Technol.*, 2021, **2**, 015016.

22 Z. Li, J. R. Kermode and A. De Vita, *Phys. Rev. Lett.*, 2015, **114**, 096405.

23 S. Chmiela, A. Tkatchenko, H. E. Sauceda, I. Poltavsky, K. T. Schütt and K.-R. Müller, *Sci. Adv.*, 2017, **3**, e1603015.

24 K. T. Schütt, M. Gastegger, A. Tkatchenko, K. R. Müller and R. J. Maurer, *Nat. Commun.*, 2019, **10**, 1–10.

25 K. T. Schütt, P. Kessel, M. Gastegger, K. A. Nicoli, A. Tkatchenko and K. R. Müller, *J. Chem. Theory Comput.*, 2019, **15**, 448–455.

26 F. Noé, A. Tkatchenko, K.-R. Müller and C. Clementi, *Annu. Rev. Phys. Chem.*, 2020, **71**, 361–390.

27 M. Bogojeski, L. Vogt-Maranto, M. E. Tuckerman, K.-R. Müller and K. Burke, *Nat. Commun.*, 2020, **11**, 1–11.

28 W. Fu and W. S. Hopkins, *J. Phys. Chem. A*, 2018, **122**, 167–171.

29 K. Ghosh, A. Stuke, M. Todorović, P. B. Jørgensen, M. N. Schmidt, A. Vehtari and P. Rinke, *Adv. Sci.*, 2019, **6**, 1801367.

30 W. Hu, S. Ye, Y. Zhang, T. Li, G. Zhang, Y. Luo, S. Mukamel and J. Jiang, *J. Phys. Chem. Lett.*, 2019, **10**, 6026–6031.

31 Y. Zhang, Q. Tang, Y. Zhang, J. Wang, U. Stimming and A. A. Lee, *Nat. Commun.*, 2020, **11**, 1–6.

32 B. X. Xue, M. Barbatti and P. O. Dral, *J. Phys. Chem. A*, 2020, **124**, 7199–7210.

33 J. Westermayr, M. Gastegger, M. F. Menger, S. Mai, L. González and P. Marquetand, *Chem. Sci.*, 2019, **10**, 8100–8107.

34 J. Westermayr and P. Marquetand, *Mach. Learn.: Sci. Technol.*, 2020, **1**, 043001.

35 J. Westermayr, F. A. Faber, A. S. Christensen, O. A. von Lilienfeld and P. Marquetand, *Mach. Learn.: Sci. Technol.*, 2020, **1**, 025009.

36 J. Westermayr, P. Marquetand and P. Marquetand, *J. Chem. Phys.*, 2020, **153**, 154112.

37 J. Westermayr, M. Gastegger, K. T. Schütt and R. J. Maurer, *J. Chem. Phys.*, 2021, **154**, 230903.

38 J. Westermayr and R. J. Maurer, *Chem. Sci.*, 2021, **12**, 10755–10764.

39 T. Mizoguchi and S. Kiyohara, *Microscopy*, 2020, **69**, 92–109.

40 Z. Chen, N. Andrejevic, N. C. Drucker, T. Nguyen, R. P. Xian, T. Smidt, Y. Wang, R. Ernstorfer, D. A. Tennant and M. Chan, *et al.*, *Chem. Phys. Rev.*, 2021, **2**, 031301.

41 C. A. Meza Ramirez, M. Greenop, L. Ashton and I. U. Rehman, *Appl. Spectrosc. Rev.*, 2021, **56**, 733–763.

42 C. D. Rankine and T. J. Penfold, *J. Phys. Chem. A*, 2021, **125**, 4276–4293.

43 C. D. Rankine, M. M. Madkhali and T. J. Penfold, *J. Phys. Chem. A*, 2020, **124**, 4263–4270.

44 M. M. Madkhali, C. D. Rankine and T. J. Penfold, *Molecules*, 2020, **25**, 2715.

45 M. M. Madkhali, C. D. Rankine and T. J. Penfold, *Phys. Chem. Chem. Phys.*, 2021, **23**, 9259–9269.

46 E. Falbo, C. Rankine and T. Penfold, *Chem. Phys. Lett.*, 2021, **780**, 138893.

47 C. Rankine and T. J. Penfold, *J. Chem. Phys*, 2022, DOI: **10.1063/5.0087255**.

48 M. R. Carbone, S. Yoo, M. Topsakal and D. Lu, *Phys. Rev. Mater.*, 2019, **3**, 033604.

49 M. R. Carbone, M. Topsakal, D. Lu and S. Yoo, *Phys. Rev. Lett.*, 2020, **124**, 156401.

This journal is © the Owner Societies 2022

Phys. Chem. Chem. Phys., 2022, **24**, 9156–9167 | 9165

50 K. Mathew, C. Zheng, D. Winston, C. Chen, A. Dozier, J. J. Rehr, S. P. Ong and K. A. Persson, *Sci. Data*, 2018, **5**, 108151.

51 C. Zheng, K. Mathew, C. Chen, Y. Chen, H. Tang, A. Dozier, J. J. Kas, F. D. Vila, J. J. Rehr, L. F. J. Piper, K. A. Persson and S. P. Ong, *npj Comput. Mater.*, 2018, **4**, 12.

52 C. Zheng, C. Chen, Y. Chen and S. P. Ong, *Patterns*, 2020, **1**, 100013.

53 J. Timoshenko, D. Lu, Y. Lin and A. I. Frenkel, *J. Phys. Chem. Lett.*, 2017, **8**, 5091–5098.

54 J. Timoshenko, A. Halder, B. Yang, S. Seifert, M. J. Pellin, S. Vajda and A. I. Frenkel, *J. Phys. Chem. C*, 2018, **122**, 21686–21693.

55 J. Timoshenko, M. Ahmadi and B. R. Cuenya, *J. Phys. Chem. C*, 2019, **123**, 20594–20604.

56 M. Ahmadi, J. Timoshenko, F. Behafarid and B. R. Cuenya, *J. Phys. Chem. C*, 2019, **123**, 10666–10676.

57 J. Timoshenko, C. J. Wrasman, M. Luneau, T. Shirman, M. Cargnello, S. R. Bare, J. Aizenberg, C. M. Friend and A. I. Frenkel, *Nano Lett.*, 2019, **19**, 520–529.

58 J. Timoshenko and A. I. Frenkel, *ACS Catal.*, 2019, **9**, 10192–10211.

59 I. Miyazato, L. Takahashi and K. Takahashi, *Mol. Syst. Des. Eng.*, 2019, **4**, 1014–1018.

60 S. B. Torrisi, M. R. Carbone, B. A. Rohr, J. H. Montoya, Y. Ha, J. Yano, S. K. Suram and L. Hung, *npj Comput. Mater.*, 2020, **6**, 1–11.

61 A. Martini, S. Guda, A. Guda, G. Smolentsev, A. Algasov, O. Usoltsev, M. A. Soldatov, A. Bugaev, Y. Rusalev and C. Lamberti, *et al.*, *Comput. Phys. Commun.*, 2020, **250**, 107064.

62 A. A. Guda, S. A. Guda, A. Martini, A. L. Bugaev, M. A. Soldatov, A. V. Soldatov and C. Lamberti, *Radiat. Phys. Chem.*, 2020, **175**, 108430.

63 S. A. Guda, A. S. Algasov, A. A. Guda, A. Martini, A. N. Kravtsova, A. L. Bugaev, L. V. Guda and A. V. Soldatov, *J. Surf. Invest.: X-Ray, Synchrotron Neutron Tech.*, 2021, **15**, 934–938.

64 D. Y. Kirsanova, M. A. Soldatov, Z. M. Gadzhimagomedova, D. M. Pashkov, A. V. Chernov, M. A. Butakova and A. V. Soldatov, *J. Surf. Invest.: X-Ray, Synchrotron Neutron Tech.*, 2021, **15**, 485–494.

65 S. Kiyohara and T. Mizoguchi, *J. Phys. Soc. Jpn.*, 2020, **89**, 103001.

66 R. M. Van der Veen, J. J. Kas, C. J. Milne, V.-T. Pham, A. El Nahhas, F. A. Lima, D. A. Vithanage, J. J. Rehr, R. Abela and M. Chergui, *Phys. Chem. Chem. Phys.*, 2010, **12**, 5551–5561.

67 J. Vinson, J. Rehr, J. Kas and E. Shirley, *Phys. Rev. B: Condens. Matter Mater. Phys.*, 2011, **83**, 115106.

68 J. Vinson and J. Rehr, *Phys. Rev. B: Condens. Matter Mater. Phys.*, 2012, **86**, 195135.

69 I. Josefsson, K. Kunnus, S. Schreck, A. Föhlisch, F. de Groot, P. Wernet and M. Odelius, *J. Phys. Chem. Lett.*, 2012, **3**, 3565–3570.

70 R. V. Pinjari, M. G. Delcey, M. Guo, M. Odelius and M. Lundberg, *J. Chem. Phys.*, 2014, **141**, 124116.

71 D. Maganas, M. Roemelt, T. Weyhermüller, R. Blume, M. Hävecker, A. Knop-Gericke, S. DeBeer, R. Schlögl and F. Neese, *Phys. Chem. Chem. Phys.*, 2014, **16**, 264–276.

72 J. Lüder, J. Schött, B. Brena, M. W. Haverkort, P. Thunström, O. Eriksson, B. Sanyal, I. Di Marco and Y. O. Kvashnin, *Phys. Rev. B*, 2017, **96**, 245131.

73 J. M. Kasper, T. F. Stetina, A. J. Jenkins and X. Li, *Chem. Phys. Rev.*, 2020, **1**, 011304.

74 J. Lüder, 2021, arXiv, arXiv:2107.13149.

75 J. Lüder, *Phys. Rev. B*, 2021, **103**, 045140.

76 D. Balcells and B. B. Skjelstad, *J. Chem. Inf. Model.*, 2020, **60**, 6135–6146.

77 Quantum Machine, 2021, quantum-machine.org/datasets.

78 O. Bunău and Y. Joly, *J. Phys.: Condens. Matter*, 2009, **21**, 345501.

79 O. Bunău, A. Y. Ramos and Y. Joly, *International Tables for Crystallography, vol. I: X-ray Absorption Spectroscopy and Related Techniques*, 2021.

80 J. Wood and A. M. Boring, *Phys. Rev. B: Solid State*, 1978, **18**, 2701–2711.

81 M. Seah and W. Dench, *NPL Report Chem.*, 1978, **82**, 1.

82 XANESNET, 2021, **gitlab.com/conor.rankine/xanesnet, commit:aca0407d**.

83 M. Gastegger, L. Schwiedrzik, M. Bittermann, F. Berzsenyi and P. Marquetand, *J. Chem. Phys.*, 2018, **148**, 241709.

84 M. Abadi, A. Agarwal, P. Barham, E. Brevdo, Z. Chen, C. Citro, G. S. Corrado, A. Davis, J. Dean and M. Devin, *et al.*, *TensorFlow: Large-Scale Machine Learning on Heterogeneous Distributed Systems*, 2015, **tensorflow.org/**.

85 Keras, **github.com/keras-team/keras**, 2015.

86 F. Pedregosa, G. Varoquaux, A. Gramfort, V. Michel, B. Thirion, O. Grisel, M. Blondel, P. Prettenhofer, R. Weiss and V. Dubourg, *et al.*, *J. Mach. Learn. Res.*, 2011, **12**, 2825–2830.

87 A. Hjorth Larsen, J. Jorgen Mortensen, J. Blomqvist, I. E. Castelli, R. Christensen, M. Dułak, J. Friis, M. N. Groves, B. Hammer and C. Hargus, *et al.*, *J. Phys.: Condens. Matter*, 2017, **29**, 273002.

88 M. Dewar, *Bull. Soc. Chim. Fr.*, 1951, **18**, C71–C79.

89 J. Chatt and L. Duncanson, *J. Chem. Soc.*, 1953, 2939–2947.

90 R. K. Hocking, E. C. Wasinger, F. M. de Groot, K. O. Hodgson, B. Hedman and E. I. Solomon, *J. Am. Chem. Soc.*, 2006, **128**, 10442–10451.

91 R. K. Hocking, E. C. Wasinger, Y.-L. Yan, F. M. Degroot, F. A. Walker, K. O. Hodgson, B. Hedman and E. I. Solomon, *J. Am. Chem. Soc.*, 2007, **129**, 113–125.

92 M. Lundberg, T. Kroll, S. DeBeer, U. Bergmann, S. A. Wilson, P. Glatzel, D. Nordlund, B. Hedman, K. O. Hodgson and E. I. Solomon, *J. Am. Chem. Soc.*, 2013, **135**, 17121–17134.

93 G. Bombieri, E. Forsellini, C. Panattoni, R. Graziani and G. Bandoli, *J. Chem. Soc. A*, 1970, 1313–1318.

94 P.-T. Cheng and S. Nyburg, *Can. J. Chem.*, 1972, **50**, 912–916.

95 G. H. Dias, N. F. d. Fonseca and M. H. Herbst, *J. Braz. Chem. Soc.*, 2012, **23**, 32–38.

9166 | *Phys. Chem. Chem. Phys.*, 2022, **24**, 9156–9167

This journal is © the Owner Societies 2022

96 B. Qi, I. Perez, P. Ansari, F. Lu and M. Croft, *Phys. Rev. B: Condens. Matter Mater. Phys.*, 1987, **36**, 2972–2975.

97 T. Sham, *Phys. Rev. B: Condens. Matter Mater. Phys.*, 1985, **31**, 1888–1902.

98 V. Briois, P. Sainctavit, G. J. Long and F. Grandjean, *Inorg. Chem.*, 2001, **40**, 912–918.

99 A. El Nahhas, R. Van Der Veen, T. Penfold, V. Pham, F. Lima, R. Abela, A. Blanco-Rodriguez, S. Zalis, A. Vlcek and I. Tavernelli, *et al.*, *J. Phys. Chem. A*, 2013, **117**, 361–369.

100 J. V. Lockard, A. A. Rachford, G. Smolentsev, A. B. Stickrath, X. Wang, X. Zhang, K. Atenkoffer, G. Jennings, A. Soldatov and A. L. Rheingold, *et al.*, *J. Phys. Chem. A*, 2010, **114**, 12780–12787.

101 R. M. Van Der Veen, C. J. Milne, A. El Nahhas, F. A. Lima, V.-T. Pham, J. Best, J. A. Weinstein, C. N. Borca, R. Abela and C. Bressler, *et al.*, *Angew. Chem.*, 2009, **121**, 2749–2752.

102 T. J. Penfold, B. F. Curchod, I. Tavernelli, R. Abela, U. Rothlisberger and M. Chergui, *Phys. Chem. Chem. Phys.*, 2012, **14**, 9444–9450.

103 K. Haldrup, G. Levi, E. Biasin, P. Vester, M. G. Laursen, F. Beyer, K. S. Kjær, T. B. Van Driel, T. Harlang and A. O. Dohn, *et al.*, *Phys. Rev. Lett.*, 2019, **122**, 063001.

104 N. P. Weingartz, M. W. Mara, S. Roy, J. Hong, A. Chakraborty, S. E. Brown-Xu, B. T. Phelan, F. N. Castellano and L. X. Chen, *J. Phys. Chem. A*, 2021, **125**, 8891–8898.

105 T. J. Penfold, C. J. Milne and M. Chergui, *Adv. Chem. Phys.*, 2013, **153**, 1–41.

106 C. Milne, T. Penfold and M. Chergui, *Coord. Chem. Rev.*, 2014, **277**, 44–68.

107 M. Bauer, *Phys. Chem. Chem. Phys.*, 2014, **16**, 13827–13837.

108 Y. Chen, C. Chen, C. Zheng, S. Dwaraknath, M. K. Horton, J. Cabana, J. Rehr, J. Vinson, A. Dozier and J. J. Kas, *et al.*, *Sci. Data*, 2021, **8**, 1–8.

This journal is © the Owner Societies 2022

Phys. Chem. Chem. Phys., 2022, **24**, 9156–9167 | 9167